Hub vortex instability within wind turbine wakes: Effects of wind turbulence, loading conditions, and blade aerodynamics

Ryan Ashton,[1] Francesco Viola,[2] Simone Camarri,[3]
Francois Gallaire,[2] and Giacomo Valerio Iungo[1,*]
[1]*University of Texas at Dallas, Mechanical Engineering Department, Wind Fluids and Experiments Lab (WindFluX), Richardson, Texas 75080, USA*
[2]*Ecole Polytechnique Fédérale de Lausanne (EPFL), Laboratory of Fluid Mechanics and Instabilities (LFMI), Lausanne, Switzerland*
[3]*Department of Civil and Industrial Engineering, University of Pisa, Pisa, Italy*
(Received 5 May 2016; published 8 November 2016)

The near wake of wind turbines is characterized by the presence of the hub vortex, which is a coherent vorticity structure generated from the interaction between the root vortices and the boundary layer evolving over the turbine nacelle. By moving downstream, the hub vortex undergoes an instability with growth rate, azimuthal and axial wavenumbers determined by the characteristics of the incoming wind and turbine aerodynamics. Thus, a large variability of the hub vortex instability is expected for wind energy applications with consequent effects on wake downstream evolution, wake interactions within a wind farm, power production, and fatigue loads on turbines invested by wakes generated upstream. In order to predict characteristics of the hub vortex instability for different operating conditions, linear stability analysis is carried out by considering different statistics of the incoming wind turbulence, thrust coefficient, tip speed ratio, and blade lift distribution of a wind turbine. Axial and azimuthal wake velocity fields are modeled through Carton-McWilliams velocity profiles by mimicking the presence of the hub vortex, helicoidal tip vortices, and matching the wind turbine thrust coefficient predicted through the actuator disk model. The linear stability analysis shows that hub vortex instability is strongly affected by the wind turbine loading conditions, and specifically it is promoted by a larger thrust coefficient. A higher load of the wind turbines produces an enhanced axial velocity deficit and, in turn, higher shear in the radial direction of the streamwise velocity. The axial velocity shear within the turbine wake is also the main physical mechanism promoting the hub vortex instability when varying the lift distribution over the blade span for a specific loading condition. Cases with a larger velocity deficit in proximity of the wake center and less aerodynamic load towards the blade tip result to be more unstable. Moreover, wake swirl promotes hub vortex instability, and it can also affect the azimuthal wave number of the most unstable mode. Finally, higher Reynolds stresses and turbulent eddy viscosity decrease both growth rate and azimuthal wave number of the most unstable mode.

DOI: 10.1103/PhysRevFluids.1.073603

I. INTRODUCTION

Wind turbine wakes are complex, multiscale flows with characteristic length scales varying from the height of the atmospheric boundary layer to the rotor diameter, which is the characteristic dimension for the wake cross-width, to the size of the different wake vorticity structures, down to small turbulent eddies governing energy dissipation [1,2]. These different length scales dominate the wake flow during the different stages of its downstream evolution [3]. At the rotor disk, wind turbine performance is affected by the characteristics of the incoming atmospheric boundary layer and lift distribution over the blade span [4]. At the region just downstream to the rotor disk, the

*valerio.iungo@utdallas.edu; www.utdallas.edu/windflux

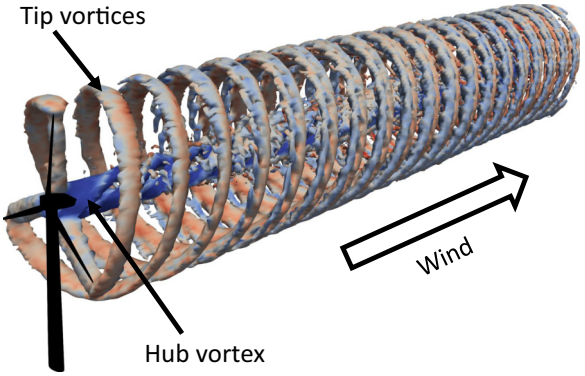

FIG. 1. Visualization from LES of tip vortices and hub vortex in a wind turbine wake (isosurface of vorticity magnitude colored with streamwise vorticity).

rollup of the wake vorticity structures takes place. Tip vortices are shed from the tip of each blade, as depicted in Fig. 1, which are then advected downstream forming a complex system of helicoidal vortices [5]. At the wake center, the interaction between the root vortices shed from the blades and the boundary layer evolving over the turbine nacelle leads to the generation of the hub vortex, as shown in Fig. 1 [6,7].

In the far wake, these coherent vorticity structures are completely diffused, and only a swirling Gaussian-like wake is observed [8]. The region connecting the near wake with the far-wake, denoted as transition region, is still not clearly characterized, as far as its streamwise extent and the prevailing physical phenomena are concerned [9–11]. In the transition region, the helicoidal tip vortices undergo different instabilities, which highly affect downstream evolution and dissipation rate of the tip vortices [6,12–17]. Recent stability analysis also showed that the hub vortex is unstable and characterized by a single-helix counterwinding instability [18–20]. The same phenomenon was then confirmed by LES simulations of a hydrokinetic turbine [10] and through water tunnel experiments of a down-scaled wind turbine model [21]. In Iungo *et al.* [18], temporal stability analysis was performed by using as base flow the time-averaged velocity field measured through wind tunnel experiments of a down-scaled wind turbine model. The temporal stability analysis carried out at several downstream locations within the turbine wake showed the presence of a single-helix instability of the hub vortex, which was then confirmed by the spatial stability analysis. The helicoidal instability predicted through the stability analysis was then corroborated through simultaneous hot-wire measurements confirming the predicted azimuthal wave number, axial wave number, and frequency of the hub vortex instability.

The coherent velocity fluctuations produced by the hub vortex instability modify significantly the downstream evolution of the hub vortex and interactions with the surrounding helicoidal tip vortices, which is considered a crucial mechanism for downstream recovery of the entire wind turbine wake [9,10,18,19]. In Ref. [11], the hub vortex instability is considered to be a source for augmenting intensity and spatial extent of wake meandering in the far wake. Therefore, it is evident that the complexity of the flow dynamics occurring in the transition region makes the prediction of the evolution between near wake and far wake a very challenging task.

The scenario related to the flow in a wind turbine wake becomes even more complicated if the variability connected with the different atmospheric conditions and operational regimes is considered. Indeed, pitch and yaw angles of a turbine are continuously adjusted as a function of the wind velocity and direction. Moreover, characteristics of the incoming boundary layer, such as wind turbulence intensity, shear, veer, and atmospheric stability can significantly affect wind turbine power performance and, in turn, the generated wakes. Recent wind LiDAR measurements

of utility-scale wind turbines performed under different atmospheric stability regimes showed that wind turbine wakes recover faster under convective regimes than for neutral ones [22,23].

This study aims to predict the characteristics of the hub vortex instability, such as growth rate, azimuthal and axial wavenumbers, for different loading conditions of a wind turbine, namely, thrust coefficient and tip speed ratio (i.e., the ratio between the rotational velocity at the blade tip and the incoming velocity at hub height), different blade aerodynamics, and turbulence characteristics of the incoming wind. This survey might be prohibitive to be carried out through wind tunnel experiments or numerical simulations due to the large number of configurations to be tested. To overcome this limitation, the wake velocity field at a reference downstream location is modeled through multiple Carton-McWilliams vortices [24], mimicking the presence of the hub vortex and tip vortices. Following a previous work on the hub vortex instability [25], for different loading conditions and tip speed ratios the radial distribution of the velocity field is obtained through an iterative method in order to match the thrust coefficient of the wind turbine predicted via an actuator disk model. The different wake velocity profiles are then analyzed via temporal linear stability analysis following the formulation proposed in Viola *et al.* [19], for which a mixing length model was used in order to take the turbulence effects into account for the prediction of wake instability. Specifically, in this paper the hub vortex instability is predicted for different characteristics of the incoming wind turbulence, induction factor, i.e., thrust coefficient of the turbine, tip speed ratio, and lift distribution over the blade span.

The remainder of the paper is organized as follows. The formulation of the linear stability analysis, including turbulence effects with a mixing length model [19], is briefly summarized in Sec. II. Then the iterative method adopted to evaluate the wake velocity profiles for different turbine loading conditions is described in Sec. III. Results of the stability analysis obtained by varying the mixing length of the turbulence model are discussed in detail in Sec. IV. Results of the stability analysis are also reported for different wind turbine induction factors and tip speed ratios in Sec. V and for different lift distributions in Sec. VI. Finally, concluding remarks are summarized in Sec. VII.

II. LINEAR STABILITY ANALYSIS WITH EDDY-VISCOSITY MODEL

The 3D velocity field $\mathbf{U}(\mathbf{x},t)$ (where $\mathbf{x} = (x,r,\theta)$ is the position vector in cylindrical coordinates and t is time) is decomposed by means of the so-called triple decomposition [26] in the time-averaged base flow, $\overline{\mathbf{U}}(\mathbf{x})$, the coherent velocity fluctuations, $\tilde{\mathbf{u}}(\mathbf{x},t)$, and the turbulent motion, $\mathbf{u}'(\mathbf{x},t)$:

$$\mathbf{U} = \overline{\mathbf{U}} + \tilde{\mathbf{u}} + \mathbf{u}', \tag{1}$$

where the sum of the time-averaged flow and the coherent fluctuations coincides with the ensemble-averaged flow $\langle \mathbf{U} \rangle = \overline{\mathbf{U}} + \tilde{\mathbf{u}}$ [27].

The flow field is considered to be unstable (stable) in the case the amplitude of $\tilde{\mathbf{u}}$ grows (decays) in time and space. Thus, stability can be verified by a modal analysis of the linearized dynamics of $\tilde{\mathbf{u}}$. To this purpose, the nonlinear evolution of the coherent perturbation for an incompressible flow can be written as [26]

$$\nabla \cdot \tilde{\mathbf{u}} = 0, \quad \frac{\partial \tilde{\mathbf{u}}}{\partial t} + \nabla \tilde{\mathbf{u}} \cdot \overline{\mathbf{U}} + \nabla \overline{\mathbf{U}} \cdot \tilde{\mathbf{u}} = -\nabla \tilde{p} + \frac{1}{\mathrm{Re}} \Delta \tilde{\mathbf{u}} - \nabla \cdot [\tilde{\mathbf{u}}\tilde{\mathbf{u}} - \overline{\tilde{\mathbf{u}}\tilde{\mathbf{u}}}] - \nabla \cdot [\langle \mathbf{u}'\mathbf{u}' \rangle - \overline{\mathbf{u}'\mathbf{u}'}], \tag{2}$$

where p represents pressure. The Reynolds number is defined by means of the time-averaged velocity at hub height and the rotor diameter, d, and is equal to 72 000 as for our reference wind tunnel experiments [18,19]. In the framework of a linear analysis with respect to the coherent fluctuations $\tilde{\mathbf{u}}$, the third term of the right-hand side of Eq. (2) is neglected. However, the system of equations is not closed, and the last term of the right-hand side of Eq. (2), which is related to the turbulent diffusion, has to be modeled. In Viola *et al.* [19], this term was modeled via Boussinesq hypothesis [26,28], and the Reynolds stresses, $\overline{R}$, are linearly proportional to the strain rate tensor, $\overline{S}$, producing

$$\overline{R} = \overline{\mathbf{u}'\mathbf{u}'} \simeq -2\nu_t \overline{S} + \tfrac{2}{3}\overline{q} I, \tag{3}$$

where $\overline{q}$ is the turbulent kinetic energy, and I is the 3×3 identity matrix.

As is well documented by several wind tunnel and LES experiments [18,29–31], the wake flow produced by a wind turbine invested by a uniform incoming velocity is practically axisymmetric, $\partial\overline{\mathbf{U}}/\partial\theta \approx 0$, with a negligible radial velocity, $\overline{U}_r \approx 0$, and slowly varying in the streamwise direction, $\partial\overline{\mathbf{U}}/\partial x \ll \partial\overline{\mathbf{U}}/\partial r$. Such a velocity field entails that $\overline{R}_{x\theta} = \overline{u'_\theta u'_x}$ is practically null, and the only significant components of the Reynolds stress tensor are then $\overline{R}_{r\theta}$, $\overline{R}_{rx}$, and their symmetric counterparts [32].

In this work, a generalized mixing-length model for swirling flows is considered [33]:

$$\nu_t(r) = l_m^2(2\overline{S} : \overline{S})^{1/2} = l_m^2\left\{\left[r\frac{\partial}{\partial r}\left(\frac{\overline{U}_\theta}{r}\right)\right]^2 + \left(\frac{\partial \overline{U}_x}{\partial r}\right)^2\right\}^{1/2}, \tag{4}$$

where ν_t is the turbulent eddy viscosity, which is a function of the downstream and radial position, while the mixing length, l_m, is only a function of the downstream location. The mixing length model in Eq. (4) turns out to be also very practical to estimate the effects of a different turbulence intensity of the incoming wind. Indeed, as shown by previous LES simulations of wind turbine wakes consequent to different turbulence levels of the incoming wind [34], higher Reynolds stresses result from higher incoming turbulence intensity, which can be modeled with a larger turbulent eddy-viscosity according to Eq. (3), thus with a larger mixing length.

By linearizing the eddy viscosity model at first order with respect to $\tilde{\mathbf{u}}$, and further manipulating Eq. (2), we obtain (see Viola *et al.* [19] for details)

$$\begin{aligned}&\frac{\partial\tilde{\mathbf{u}}}{\partial t} + \boldsymbol{\nabla}\tilde{\mathbf{u}}\cdot\overline{\mathbf{U}} + \boldsymbol{\nabla}\overline{\mathbf{U}}\cdot\tilde{\mathbf{u}}\\ &\quad= -\boldsymbol{\nabla}\tilde{p} + \frac{1}{\mathrm{Re}}\Delta\tilde{\mathbf{u}} + \boldsymbol{\nabla}\cdot\{\nu_t(\overline{\mathbf{U}})[\boldsymbol{\nabla}+\nabla^T]\tilde{\mathbf{u}}\} + \boldsymbol{\nabla}\cdot\{[\boldsymbol{\nabla}_{\mathbf{U}}\nu_t(\overline{\mathbf{U}})\cdot\tilde{\mathbf{u}}][\boldsymbol{\nabla}+\nabla^T]\overline{\mathbf{U}}\},\end{aligned} \tag{5}$$

where the term $\nu_t(\overline{\mathbf{U}})$ in Eq. (5) can be evaluated from the statistics of the velocity field [32], while the term $\nabla_{\mathbf{U}}\nu_t(\overline{\mathbf{U}})\cdot\tilde{\mathbf{u}}$ is obtained by the linearization of the turbulence model used to close the equations. Compared to previous work [26,28,35], Eq. (5) includes the linearization of the turbulence model through the last term in the right-hand side.

In the framework of weakly nonparallel stability analysis, Eq. (5) is now applied to a parallel flow $\overline{\mathbf{U}} = (\overline{U}_x, \overline{U}_\theta, 0)$ evaluated at a given streamwise location. This allows for a modal expansion of the coherent fluctuations in the following form:

$$\tilde{\mathbf{u}}(x,\theta,r,t) = \hat{\mathbf{u}}(r)\exp(ikx + im\theta - i\omega t), \tag{6}$$

where k and m are the axial and azimuthal wave numbers, respectively, and ω is the frequency. When this modal form is substituted in Eq. (5), an eigenvalue problem is obtained. In the temporal stability analysis, k is real and assigned, ω is the complex eigenvalue of the problem, and m is a free integer parameter.

For the stability analysis, Eq. (5) together with the continuity equation are discretized using a code based on a Chebyshev spectral collocation method. In the present analysis, the number of collocation points is $N = 120$ and the size of the domain in the radial direction is $r_{\max}/d = 50$. This choice provides the convergence of the most unstable eigenvalue with a five-digit accuracy, which is sufficient for the present purposes.

III. MODELING OF THE WAKE VELOCITY PROFILES FOR DIFFERENT LOADING CONDITIONS

Temporal linear stability analysis is performed by using as base flow the wake velocity field evaluated at the turbine location, just downstream to the turbine rotor. Similarly to the actuator disk model [36], the streamwise velocity deficit and the wake swirl past the turbine are the result of the power capture exerted by the turbine. The axial velocity profile, U, representing the velocity deficit connected with the hub vortex and the time-averaged footprint of the helicoidal tip vortices,

is modeled through Gaussian functions:

$$\frac{U(r)}{U_\infty} = 1 - U_{\text{hub}} \exp\left[-\left(\frac{r}{\sigma_{\text{hub}}}\right)^2\right] - U_{\text{tip}} \exp\left[-\left(\frac{r - r_{\text{tip}}}{\sigma_{\text{tip}}}\right)^2\right], \tag{7}$$

where U_∞ is the freestream velocity, U_{hub} is the maximum velocity deficit connected with the hub vortex, and U_{tip} is the one related to the tip vortex. The radial position from the wake center is r, while r_{tip} is the radial position of the tip vortex. The parameters σ_{hub} and σ_{tip} are proportional to the cross-dimensions of the hub and tip vortex, respectively. This strategy to model the velocity field of a wind turbine wake was already assessed by previous experimental and numerical works [8,30]. Moreover, modeling the presence of the helicoidal tip vortices produced by a three-bladed turbine with an annular distribution of streamwise vorticity has already been applied successfully for the prediction of the hub vortex instability [18,19]. This approximation is more accurate for low tip speed ratios (TSRs), which leads to a larger pitch of the helicoidal tip vortices.

From the momentum budget in the streamwise direction, the thrust coefficient of the wind turbine, C_T, can be evaluated as follows (see the Appendix for details):

$$C_T = \frac{8}{R^2} \int_0^R \frac{U}{U_\infty}\left(1 - \frac{U}{U_\infty}\right) r \, dr, \tag{8}$$

where R is the rotor radius. By injecting Eq. (7) into Eq. (8), we obtain

$$\begin{aligned} C_T = \frac{8U_{\text{hub}}}{R^2} \int_0^R & \left(1 - U_{\text{hub}}\left\{\exp\left[-\left(\frac{r}{\sigma_{\text{hub}}}\right)^2\right] - k_U \exp\left[-\left(\frac{r - r_{\text{tip}}}{\sigma_{\text{tip}}}\right)^2\right]\right\}\right) \\ & \times \left\{\exp\left[-\left(\frac{r}{\sigma_{\text{hub}}}\right)^2\right] + k_U \exp\left[-\left(\frac{r - r_{\text{tip}}}{\sigma_{\text{tip}}}\right)^2\right]\right\} r \, dr, \end{aligned} \tag{9}$$

where $k_U = U_{\text{tip}}/U_{\text{hub}}$ (see the Appendix for the derivation).

The azimuthal velocity profile, V_θ, is modeled through Carton-McWilliams vortices [24], which is a model previously used to investigate instabilities of swirling jets [37], and to describe the plane instabilities of the so-called isolated or screened vortices, i.e., vortices with circulation decreasing away from the core [38,39]. The azimuthal velocity is expressed as follows:

$$\frac{V_\theta(r)}{U_\infty} = \Omega_{\text{hub}} r \exp\left[-\left(\frac{r}{\sigma_{\theta,\text{hub}}}\right)^\alpha\right] - \Omega_{\text{tip}}(r - r_{\text{tip}}) \exp\left[-\left(\frac{r - r_{\text{tip}}}{\sigma_{\theta,\text{tip}}}\right)^\alpha\right], \tag{10}$$

where Ω_{hub} is the axial vorticity peak of the hub vortex, while Ω_{tip} is the one for the tip vortex. The parameters $\sigma_{\theta,\text{hub}}$ and $\sigma_{\theta,\text{tip}}$ are proportional to the core radius of the hub and tip vortex, respectively. Variation of the free parameter α modify the radial distribution of the vorticity field.

The thrust coefficient of a wind turbine is evaluated now from the momentum budget in the azimuthal direction (see the Appendix for details):

$$C_T = \frac{4\text{TSR}}{R^3} \int_0^R \frac{V_\theta}{U_\infty}\left(1 + \frac{1}{2\text{TSR}} \frac{R}{r} \frac{V_\theta}{U_\infty}\right) r^2 \, dr. \tag{11}$$

By injecting Eq. (10) in Eq. (11), we obtain

$$\begin{aligned} C_T = \frac{4\text{TSR}\Omega_{\text{hub}}}{R^3} \int_0^R & \left\{r \exp\left[-\left(\frac{r}{\sigma_{\theta,\text{hub}}}\right)^\alpha\right] - k_\Omega (r - r_{\text{tip}}) \exp\left[-\left(\frac{r - r_{\text{tip}}}{\sigma_{\theta,\text{tip}}}\right)^\alpha\right]\right\} \\ & \times \left(1 + \frac{\Omega_{\text{hub}}}{2\text{TSR}} \frac{R}{r}\left\{r \exp\left[-\left(\frac{r}{\sigma_{\theta,\text{hub}}}\right)^\alpha\right] - k_\Omega (r - r_{\text{tip}}) \exp\left[-\left(\frac{r - r_{\text{tip}}}{\sigma_{\theta,\text{tip}}}\right)^\alpha\right]\right\}\right) r^2 \, dr, \end{aligned} \tag{12}$$

where $k_\Omega = \Omega_{\text{tip}}/\Omega_{\text{hub}}$ (see the Appendix for the derivation).

TABLE I. Parameters of the velocity profiles adopted to mimic a fixed aerodynamic design of the turbine blades.

Parameter	Value
$k_U = U_{\text{tip}}/U_{\text{hub}}$	0.33
σ_{hub}	0.26
σ_{tip}	0.087
r_{tip}	0.45
$k_\Omega = \Omega_{\text{tip}}/\Omega_{\text{hub}}$	0.25
$\sigma_{\theta,\text{hub}}$	0.26
$\sigma_{\theta,\text{tip}}$	0.065
α	2.6

According to the actuator disk model, the loading conditions of a wind turbine can be represented through the (axial) induction factor, a, which is a direct measurement of the velocity deficit produced through the turbine rotation [36]:

$$a = 1 - \frac{U_R}{U_\infty}. \tag{13}$$

U_R is the uniform axial velocity in the wake at the rotor disk location past the turbine. Consequently, the thrust coefficient, C_T, can be expressed as a function of the induction factor

$$C_T = 4a(1-a), \tag{14}$$

and the power coefficient, C_P, can be evaluated as

$$C_P = 4a(1-a)^2. \tag{15}$$

The prediction of the axial velocity field produced by wind turbines via an actuator disk model cannot be highly accurate, especially for relatively low TSRs [40]. However, this simple model can be very effective to estimate modifications of the velocity field for different loading conditions of a turbine. The robustness of the actuator disk model is proven by its extensive use for high-fidelity numerical simulations of wind turbine wakes [41–43].

For a given loading condition, i.e., induction factor and TSR, the wake velocity profiles of a wind turbine are evaluated through the iterative method that we now describe. First, all the free parameters in Eqs. (7) and (10), with the exception of the maximum axial velocity deficit located at center of the wake, U_{hub}, and the peak of the axial vorticity, Ω_{hub}, are fixed in order to mimic a certain aerodynamic design of the turbine blades. For a given incoming wind, this assumption is more accurate for relatively low angles of attack of the blade airfoils, thus far from stall conditions and operations with relatively low tip speed ratios. In this work, their respective values were selected accordingly to previous wind tunnel experiments [18,19] and are reported in Table I. A taste of the effects due to variations of the turbine aerodynamics for a given loading condition will be provided in Sec. VI by varying the parameter $k_\sigma = \sigma_{\text{hub}}/\sigma_{\text{tip}}$.

Once the induction factor, a, is fixed, the parameter U_{hub} is estimated in order to minimize the error (with five-digit accuracy) between the C_T evaluated through the momentum budget in Eq. (9) and the value predicted through the actuator disk model in Eq. (14). Therefore, the axial velocity profile is univocally estimated by selecting the induction factor, a.

A similar method is then applied for the evaluation of the azimuthal velocity, V_θ. However, in Eqs. (11) and (12) it is observed that C_T is a function of the induction factor, a, and tip speed ratio, TSR. Therefore, in order to obtain univocally V_θ, they both need to be fixed for a certain loading condition. Then, Ω_{hub} is estimated satisfying the condition that the C_T evaluated through Eq. (12) matches the value obtained through the actuator disk model in Eq. (14) and, thus, the value predicted

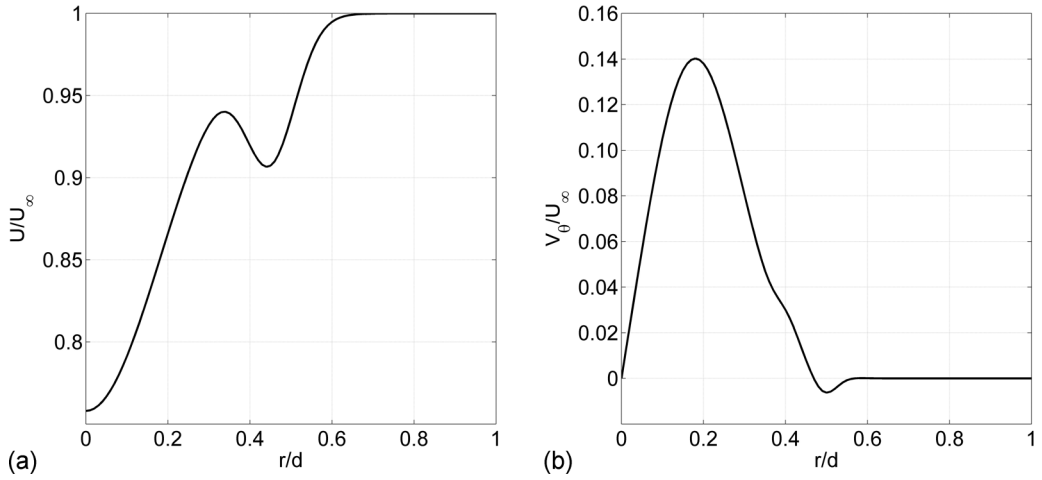

FIG. 2. Wake velocity profiles for $a = 0.1106$ and TSR $= 7$: (a) axial velocity, U/U_∞; (b) azimuthal velocity, V_θ/U_∞.

by the momentum balance in the streamwise direction, making the velocity profile consistent with Eq. (9).

IV. EFFECTS OF THE INCOMING WIND TURBULENCE

As mentioned in Sec. II, the effects of a different turbulence intensity of the incoming wind on the hub vortex instability can be investigated by varying the Reynolds stresses, thus the mixing length in Eq. (4). For this test case, a typical loading condition of a utility-scale wind turbine is simulated by using an induction factor $a = 0.1106$, which corresponds to a thrust coefficient $C_T = 0.39$ and power coefficient $C_P = 0.35$, while the TSR is TSR $= 7$. As described in the previous section, the wake velocity profiles are obtained through an iterative method in order to minimize with five-digit accuracy the difference between the thrust coefficient evaluated through the momentum budget in Eqs. (9) and (12), and the one predicted with the actuator disk model in Eq. (14). The resulting wake velocity profiles, which are shown in Fig. 2, qualitatively reproduce the typical wind turbine wake flow obtained through wind tunnel experiments [18,19] and LES simulations [29]. The axial velocity profile presents a significant velocity deficit in correspondence of the wake center, which is connected with the presence of the hub vortex. In proximity of the tip vortex, i.e., for $r/d \approx 0.45$, a secondary axial velocity deficit is present. For the azimuthal velocity, the wake swirl induced by the hub vortex exhibits a peak of the tangential velocity for the position $r/d \approx 0.2$, while the one related to the tip vortex is less predominant but still noticeable for locations close to $r/d = 0.45$.

The wake velocity field estimated for a fixed loading condition was then investigated through temporal linear stability analysis by varying the mixing length to mimic different turbulence intensities of the incoming wind ($l_m/d = 0.002, 0.004, 0.006, 0.010, 0.015$, and 0.020, values selected according to previous experimental [19] and numerical [29,34] works). The results of the stability analysis are presented as spectra where the axial wave number, k, is reported on the horizontal axis, while the growth rate, ω_i, which is the imaginary part of the pulsation defined in Eq. (6), is reported on the vertical axis. The stability spectra evaluated for different azimuthal wave numbers, m, and mixing lengths, l_m, are reported in Fig. 3. A larger mixing length, thus a higher turbulence intensity, produces an overall damping of the growth rate for all the azimuthal wave numbers. Therefore, the hub vortex instability is more likely to occur during stable atmospheric conditions, which are characterized by a relatively low wind turbulence intensity, than for convective regimes [22]. This result also indicates that the coherent velocity fluctuations produced by the hub vortex instability

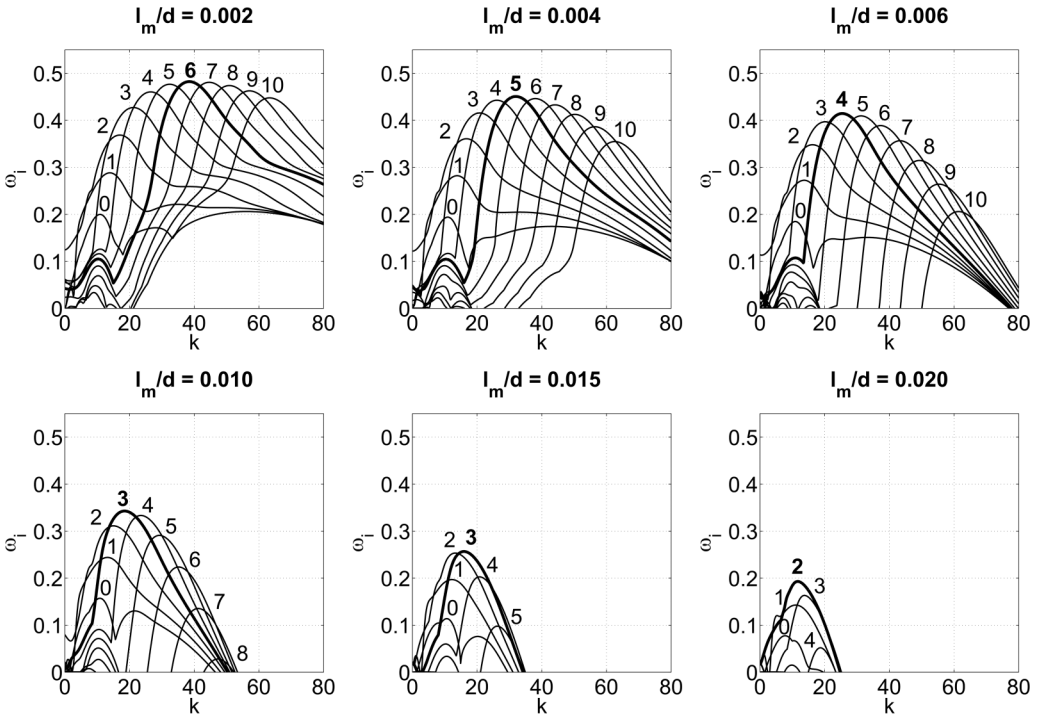

FIG. 3. Growth rate, ω_i, as a function of axial wave number, k, for various mixing lengths, l_m, and loading condition corresponding to $a = 0.1106$ and TSR $= 7$. Each curve is labeled with its azimuthal wave number and the dominant unstable mode is in bold.

may have significant consequences on turbine wake recovery and dynamic loads on downstream turbines for wind conditions characterized by a relatively low turbulence level.

For each value of the mixing length, the most unstable mode is characterized by the azimuthal wave number, m, with the largest growth rate. In Fig. 3 it is observed that as the mixing length increases the azimuthal wave number of the most unstable mode becomes smaller, with values ranging from 6 to 2 by varying the mixing length from 0.002 d up to 0.02 d. The variability of the azimuthal wave number for different mixing lengths is better appreciated in Fig. 4, where the axial vorticity of the most unstable mode is reported. For all cases the most unstable mode is detected in proximity of the wake core, indicating that the temporal stability analysis and the used wake model combine into a compelling tool to characterize the hub vortex instability. In Fig. 4 helicoidal structures with different azimuthal wave numbers are visualized for the most unstable eigenmode. A larger azimuthal wave number of the most unstable mode entails larger coherent velocity fluctuations as a consequence of the more predominant velocity gradients. Therefore, for a smaller mixing length, thus a lower turbulence intensity, the higher growth rate and a larger azimuthal wave number of the most unstable mode indicate that effects of the hub vortex instability on downstream evolution of wind turbine wakes are more significant for atmospheric stable conditions characterized by a lower wind turbulence intensity.

V. EFFECTS OF THE LOADING CONDITION

In order to evaluate effects of different loading conditions on the hub vortex stability, induction factor and TSR are varied producing different wake velocity fields. First, the induction factor is varied from 0.05 to 0.3, in order to represent power coefficients lower than the maximum value predicted through the Betz's theory [36], while keeping fixed the TSR. The corresponding range for

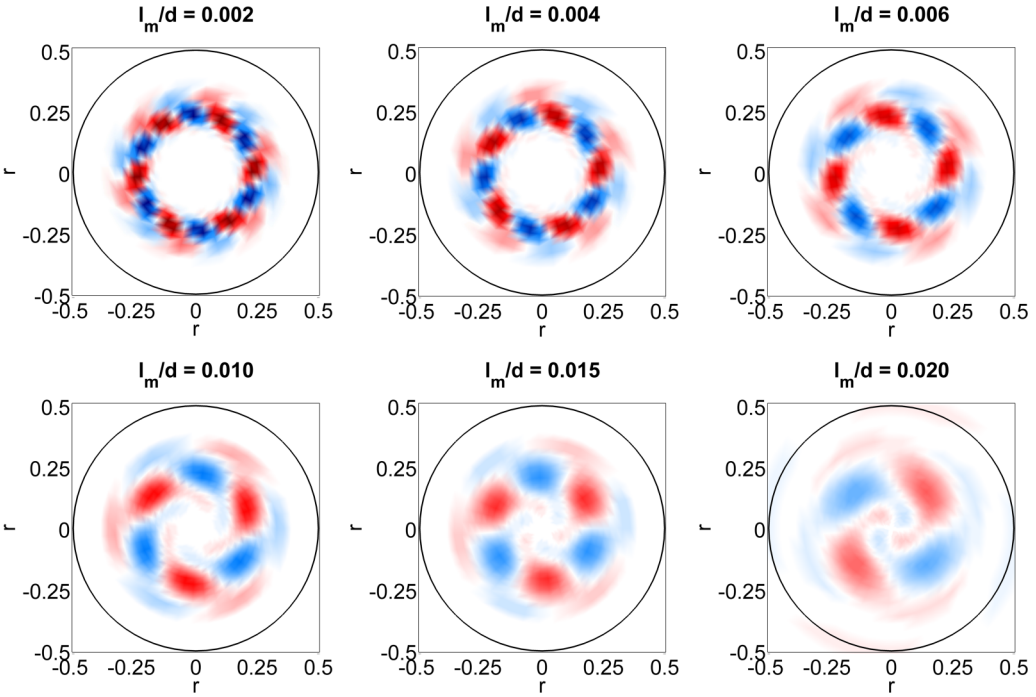

FIG. 4. Axial vorticity of the dominant unstable modes for different mixing lengths. All the figures are reported with the same color scale where blue and red represents negative and positive vorticity, respectively.

the thrust coefficient is $0.19 \leqslant C_T \leqslant 0.84$, and for the power coefficient is $0.18 \leqslant C_P \leqslant 0.59$. The TSR is set to TSR $= 8$, while the mixing length is equal to $0.02\,d$, which is consistent with typical wind turbine operations [44]. For each case, the method described in Sec. III is used to produce the corresponding wake velocity profiles for a given loading condition. The axial and azimuthal velocity profiles obtained for a fixed TSR and by varying the induction factor are reported in Fig. 5. With an increasing induction factor, both thrust and power coefficients increase according to Eqs. (14)

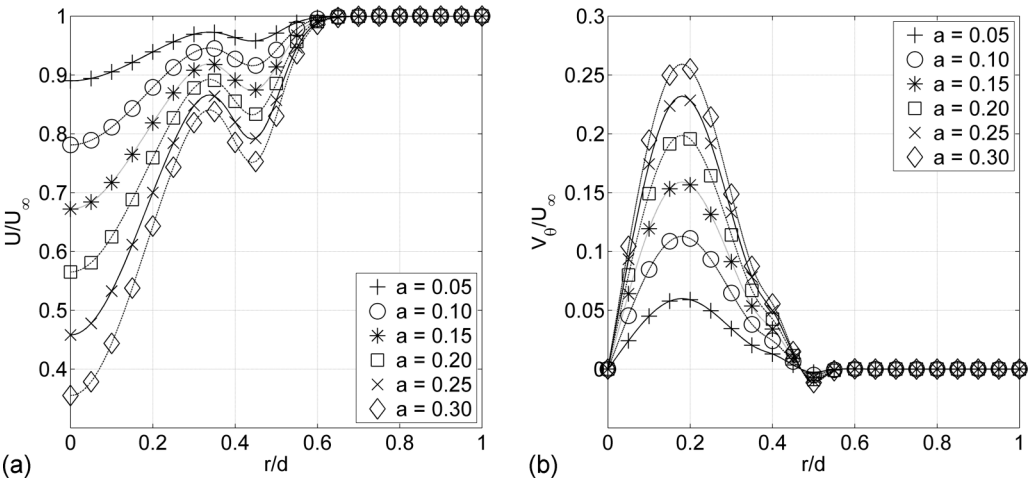

FIG. 5. Wake velocity profiles evaluated for various induction factors and TSR $= 8$: (a) axial velocity, U/U_∞; (b) azimuthal velocity, V_θ/U_∞.

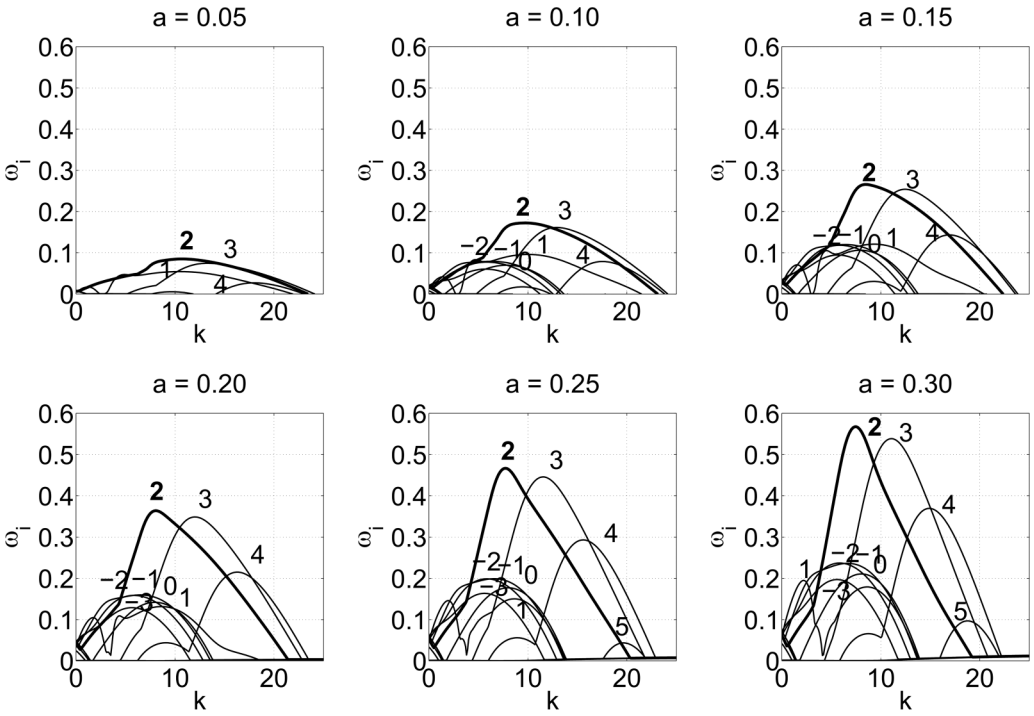

FIG. 6. Growth rate, ω_i, as a function of axial wave number k for various induction factors and TSR $= 8$. The induction factor increases from left to right, top to bottom.

and (15), and a larger wake velocity deficit is produced, as shown in Fig. 5(a). Indeed, both velocity deficits in correspondence of the hub and tip vortices are enhanced with increasing induction factor. Therefore, a general larger axial shear, i.e., the radial gradient of the axial velocity, is produced with increasing induction factor. Regarding the azimuthal velocity field, according to Eq. (11) an increased turbine thrust entails higher wake swirl, as shown in Fig. 5(b).

A temporal linear stability analysis was performed for the wake velocity profiles corresponding to the various induction factors. In Fig. 6 the stability spectra show that the growth rate is generally increased for higher induction factors, which indicates that the wake velocity deficit, an axial increased shear and an enhanced wake swirl promote hub vortex instability. Furthermore, for all considered cases, the dominant unstable mode is characterized by an azimuthal wave number $m = 2$. Therefore, the induction factor does not affect the azimuthal wave number of the most unstable mode.

The result of a dominant unstable mode characterized by a double-helix structure ($m = 2$) is in disagreement with our previous experimental investigations [18–20], for which a single-helix counterwinding ($m = 1$) unstable mode was estimated and assessed through wind tunnel experiments. The main difference between this test case with a varying induction factor and the previous wind tunnel experiment is a different tip speed ratio of the wind turbine: TSR $= 8$ has been considered for the present work, which is a typical value for utility-scale wind turbines, while for the wind tunnel experiment TSR $= 4.7$ was used. To shed some light on the effects of the tip speed ratio on the hub vortex stability, another test case was studied by varying TSR from 2 to 18, while keeping fixed the thrust to $C_T = 0.51$, i.e., by setting the induction factor to $a = 0.15$. Albeit the range of TSR values investigated is typical for utility-scale wind turbines with blade pitch control [36], this test case may sound unrealistic because for real wind turbine applications the TSR is used to set power and thrust of the turbine. However, varying the TSR for a fixed induction factor allows the modification of the azimuthal velocity field while keeping unchanged the axial velocity. Therefore, the sole effects of the wake swirl on the hub vortex stability are then investigated.

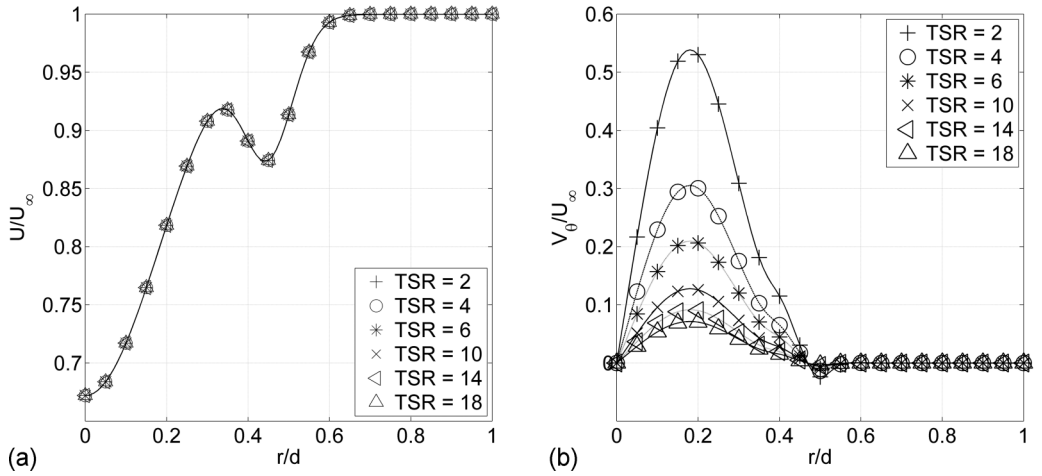

FIG. 7. Wake velocity profiles evaluated for various tip speed ratios and induction factor $a = 0.15$: (a) axial velocity, U/U_∞; (b) azimuthal velocity, V_θ/U_∞.

The variation of the TSR allows the generation of the wake velocity profiles reported in Fig. 7. According to the actuator disk model, for a fixed induction factor, C_T and C_P are constant [see Eqs. (14) and (15)], and for a certain turbine blade, i.e., by fixing the parameters k_U, σ_{hub}, σ_{tip}, and r_{tip} in Eq. (9), also the velocity deficit at the wake center, U_{hub}, is constant. Therefore, the axial velocity profile is unchanged for a fixed induction factor and varying the tip speed ratio [Fig. 7(a)].

For the azimuthal velocity reported in Fig. 7(b), a reduced tip speed ratio increases the wake swirl for a fixed induction factor. From a physical stand point, it means that a given amount of power can be harvested by spinning fast the turbine rotor with low aerodynamic load over the blades, thus producing less swirl in the wake, or vice versa with a lower tip speed ratio and higher blade aerodynamic load.

The stability spectra obtained from the temporal linear stability analysis carried out for a varying tip speed ratio are reported in Fig. 8. The growth rate is reduced for an increasing TSR, which indicates that the wake swirl promotes the hub vortex instability. Moreover, by varying the TSR, a switch from $m = 1$ to $m = 2$ is observed by increasing the TSR from 4 to 6. This result justifies the single-helix instability observed from our previous wind tunnel experiment, for which TSR $= 4.7$ was used [18–20]. Therefore, the TSR and the wake swirl can affect both growth rate and azimuthal wave number of the hub vortex instability.

To further map out the effects of loading conditions on the hub vortex stability, the characteristics of the dominant unstable mode as a function of induction factor and TSR are reported through a map in Fig. 9. In this figure, the marker color represents the frequency, ω_r, the size of the marker represents the growth rate, ω_i, while the number next to each point is the azimuthal wave number, m. Figure 9 shows that the growth rate, ω_i, increases with larger induction factor and lower TSR; thus, axial velocity deficit, i.e., axial shear, and wake swirl promote the hub vortex instability. The frequency, ω_r, is mainly affected by the TSR, and it is increased for lower TSR. Similarly, the azimuthal wave number is mainly affected by the wake swirl. A transition from $m = 1$ to $m = 2$ is observed by increasing tip speed ratio between TSR $= 4$ and TSR $= 6$. This transition region is nearly independent of the induction factor. An exception occurs for $a = 0.05$, where the dominant azimuthal wave number switches from $m = 1$ to $m = 2$ between TSR $= 6$ and 8.

To deeper analyze the effects of axial shear and wake swirl on the hub vortex stability, the results of the linear stability analysis are now reported in Fig. 10(a) as a function of the axial velocity deficit at the wake center, U_{hub}, and the maximum axial vorticity, Ω_{hub}. The ranges of these two parameters are broader than the corresponding ones in Fig. 9, which might entail that not all the considered cases correspond to realistic wind turbine operations. Figure 10(a) is analogous to Fig. 9, for both figures

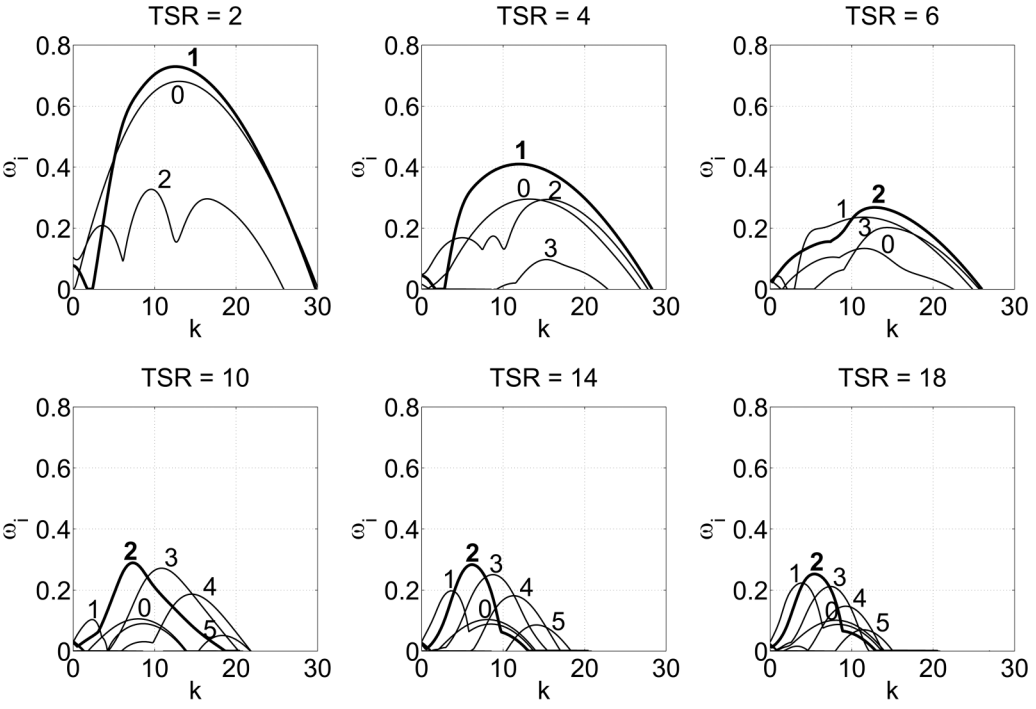

FIG. 8. Growth rate, ω_i, as a function of axial wave number, k, for various tip speed ratios and $a = 0.15$.

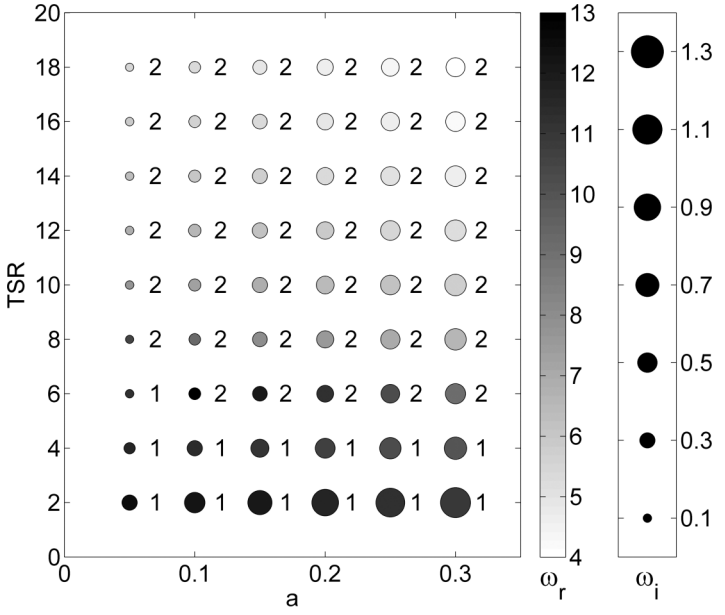

FIG. 9. Characteristics of the dominant unstable mode as a function of induction factor and TSR. The color map represents the frequency, ω_r, size of the marker represents growth rate, ω_i, and the number next to each circle is the azimuthal wave number, m.

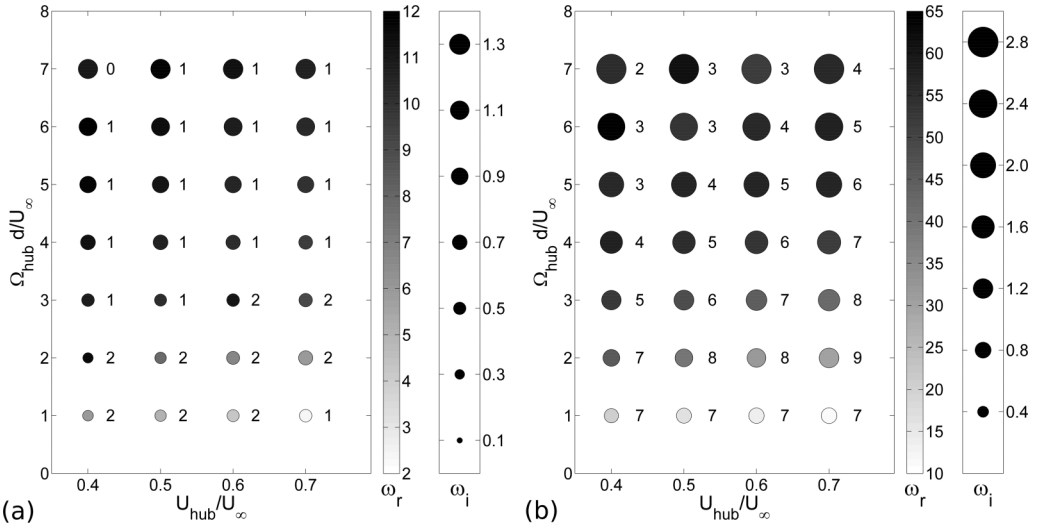

FIG. 10. Characteristics of the hub vortex instability for different axial velocity deficit at the wake center, U_{hub}, maximum axial vorticity, Ω_{hub}, and turbulent intensity of the incoming wind: (a) mixing length $l_m/d = 0.02$ and (b) mixing length $l_m/d = 0.002$. The marker color represents the frequency, ω_r, the size of the marker represents the growth rate, ω_i, while the number next to each circle is the azimuthal wave number, m.

a mixing length $l_m/d = 0.02$ is used. Once again, it is confirmed that the hub vortex instability is promoted, namely, with higher ω_i, for increased wake swirl and enhanced wake velocity deficit. A transition from $m = 1$ to $m = 2$ is generally observed with a decreasing wake swirl.

By considering a smaller mixing length, i.e., for $l_m/d = 0.002$, higher growth rate is generally obtained, as shown in Fig. 10(b), which is in agreement with the results presented in Sec. IV. Interestingly, a larger variability of the azimuthal wave number is also observed, compared to the previous case with a larger mixing length. The azimuthal wave number of the most unstable mode is generally reduced with increasing wake swirl. Moreover, a variability of m with the wake velocity deficit is now observed as well. Lower values of the azimuthal wave number are estimated for increased velocity deficit, i.e., for lower U_{hub}.

VI. EFFECTS OF VARYING THE SPANWISE LIFT DISTRIBUTION

The analysis for the prediction of the hub vortex instability has been performed by using as base flow the velocity profiles modeled through Eqs. (7) and (10), and by fixing the values of the parameters according to previous wind tunnel experiments [18,19] (Table I). However, for a given loading condition, namely, induction factor and TSR, the wake velocity field can vary for different aerodynamic design of the turbine blades, thus different distributions of the aerodynamic forces over the blade span. Therefore, a different aerodynamic design of the turbine blades can be represented through variations of the mentioned parameters.

Effects of the spanwise lift distribution on the hub vortex instability are investigated by varying the ratio $k_\sigma = \sigma_{\text{hub}}/\sigma_{\text{tip}}$ from 2 to 6. Higher values of k_σ represent cases with a larger aerodynamic load towards the blade root. The wake velocity profiles are calculated for $a = 0.1106$ and TSR $= 7$, as for Sec. IV. The obtained velocity profiles are reported in Fig. 11. With increasing k_σ, the tip vortex becomes more concentrated and extended over a narrower area. In order to keep C_T unchanged, both velocity deficits at the tip and hub vortices are consequently enhanced [Fig. 11(a)]. For the same reason, also the azimuthal velocity is slightly increased with increasing k_σ [Fig. 11(b)].

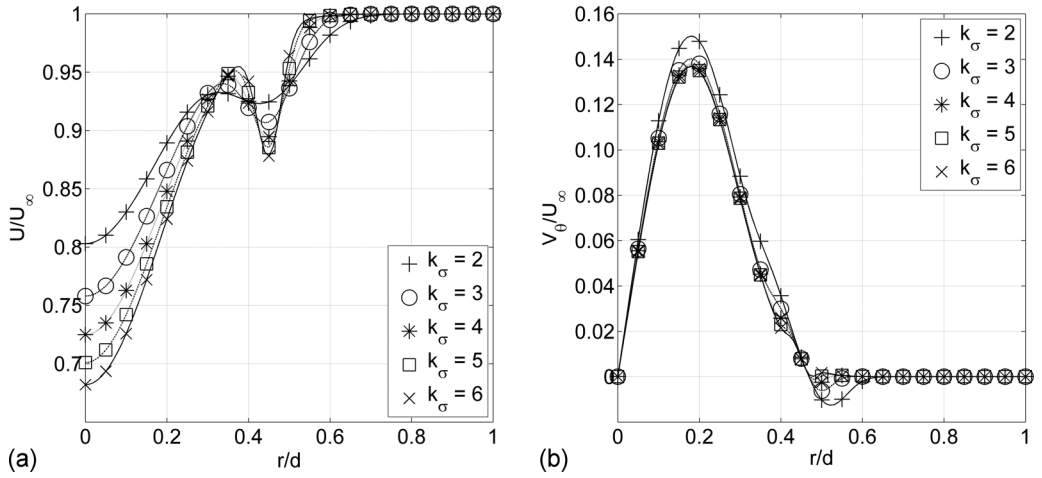

FIG. 11. Wake velocity profiles evaluated for various $k_\sigma = \sigma_{\text{hub}}/\sigma_{\text{tip}}$, $a = 0.1106$ and TSR $= 7$: (a) axial velocity, U/U_∞; (b) azimuthal velocity, V_θ/U_∞.

In Fig. 12 spectra from the stability analysis show that the growth rate of the dominant unstable mode increases with increasing k_σ. Therefore, this result confirms that lift distributions leading to larger axial velocity deficit and wake swirl promote the hub vortex instability.

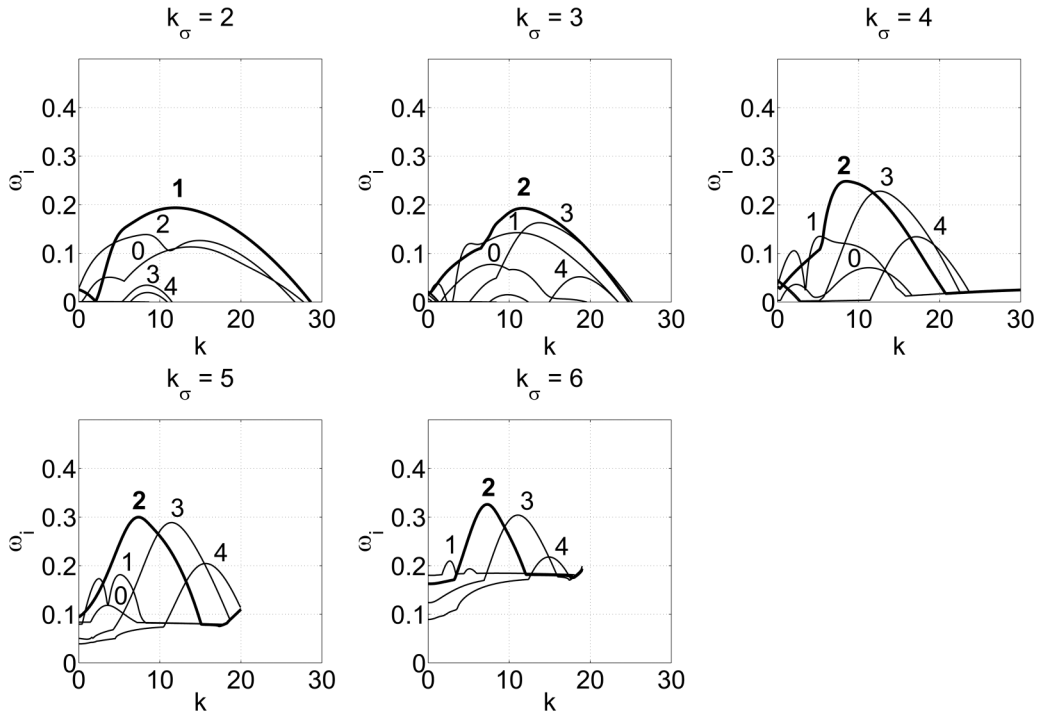

FIG. 12. Growth rate, ω_i, as a function of the axial wave number k, for various $k_\sigma = \sigma_{\text{hub}}/\sigma_{\text{tip}}$. Each curve is labeled with its azimuthal wave number. The dominant mode is in bold.

VII. CONCLUSIONS

Temporal linear stability analysis of the velocity field connected with wind turbine wakes generated for different turbulence levels of the incoming wind and loading conditions were performed to investigate the hub vortex instability. Hub vortex and tip vortices were modeled through Carton-McWilliams vortices, while wake velocity profiles were evaluated via iterative method and matching the thrust coefficient evaluated through momentum budget with the value predicted through actuator disk model.

Effects of the incoming wind turbulence on the hub vortex instability have been investigated by varying the mixing length of the turbulence model included in the stability analysis formulation. This analysis allows exploring the variability of the hub vortex instability due to different turbulence intensities of the incoming wind. However, the adopted strategy cannot explain how the large energy-containing structures present in the atmospheric boundary layer interact with the turbine rotor, thus modifying dynamics of the wake vorticity structures. Stability spectra have shown that an increased wind turbulence damps significantly the instability growth rate. Moreover, the azimuthal wave number of the most unstable mode is also decreased for an increased mixing length.

Stability analysis carried out for different loading conditions, i.e., by varying axial induction factor and TSR, has shown that hub vortex instability is promoted by the wake velocity deficit, namely, the radial shear of the axial velocity, and the wake swirl. Therefore, the growth rate increases with increasing induction factor and, for a fixed induction factor, with reducing TSR. This result has been also confirmed by keeping fixed the loading condition of the turbine and varying lift distribution. Cases with more aerodynamic load towards the blade root or producing an enhanced wake swirl promote hub vortex instability.

It has been found that the TSR has more influence on the selection of the azimuthal wave number of the dominant unstable mode than the induction factor. Specifically, a larger azimuthal wave number characterizes cases with higher TSR. However, an important role is also played by wind turbulence and, thus, by the mixing length. More significant variability has been observed for lower turbulence intensity, which also entails to higher azimuthal wave numbers.

This study suggests that for utility-scale wind turbines, the hub vortex instability is more likely to occur for wind conditions characterized by a relatively low wind turbulence intensity, such as during night time for stable atmospheric conditions. Indeed, under a stable atmospheric regime, wind turbine wakes can be extended for very long downstream distances of the order of 10–20 times the rotor diameter. Therefore, the coherent velocity fluctuations associated with the hub vortex instability might have significant effects on power losses due to wake interactions and added fatigue loads on downstream wind turbines.

ACKNOWLEDGMENTS

Stefano Leonardi, Mithu Debnath, and Christian Santoni are acknowledged for Fig. 1. TACC is acknowledged for providing computational time.

APPENDIX

According to the axial momentum budget, the thrust connected with an annular section of the actuator disk is

$$\mathrm{d}T = 2\rho U(U_\infty - U)2\pi r\, dr. \tag{A1}$$

The total thrust over the disk of radius R is then

$$T = 4\pi\rho U_\infty^2 \int_0^R \frac{U}{U_\infty}\left(1 - \frac{U}{U_\infty}\right) r\, dr. \tag{A2}$$

The thrust coefficient C_T is defined as

$$C_T = \frac{T}{\frac{1}{2}\rho U_\infty^2 \pi R^2}, \tag{A3}$$

then, by injecting Eq. (A2) into Eq. (A3), C_T can be evaluated as follows:

$$C_T = \frac{8}{R^2}\int_0^R \frac{U}{U_\infty}\left(1-\frac{U}{U_\infty}\right) r\,dr. \tag{A4}$$

By injecting Eq. (7) into Eq. (A4), we obtain

$$\begin{aligned} C_T &= \frac{8}{R^2}\int_0^R \left\{1 - U_{\text{hub}}\exp\left[-\left(\frac{r}{\sigma_{\text{hub}}}\right)^2\right] - U_{\text{tip}}\exp\left[-\left(\frac{r-r_{\text{tip}}}{\sigma_{\text{tip}}}\right)^2\right]\right\} \\ &\quad\times\left(1-\left\{1 - U_{\text{hub}}\exp\left[-\left(\frac{r}{\sigma_{\text{hub}}}\right)^2\right] - U_{\text{tip}}\exp\left[-\left(\frac{r-r_{\text{tip}}}{\sigma_{\text{tip}}}\right)^2\right]\right\}\right) r\,dr \\ &= \frac{8}{R^2}\int_0^R \left\{1 - U_{\text{hub}}\exp\left[-\left(\frac{r}{\sigma_{\text{hub}}}\right)^2\right] - U_{\text{tip}}\exp\left[-\left(\frac{r-r_{\text{tip}}}{\sigma_{\text{tip}}}\right)^2\right]\right\} \\ &\quad\times\left\{U_{\text{hub}}\exp\left[-\left(\frac{r}{\sigma_{\text{hub}}}\right)^2\right] + U_{\text{tip}}\exp\left[-\left(\frac{r-r_{\text{tip}}}{\sigma_{\text{tip}}}\right)^2\right]\right\} r\,dr, \end{aligned} \tag{A5}$$

which leads to Eq. (9) by defining $k_U = U_{\text{tip}}/U_{\text{hub}}$.

Considering the azimuthal momentum budget, the thrust of an annular element is [45]:

$$dT = 2\pi\rho\left(\Omega + \frac{\omega}{2}\right)\omega r^3\,dr, \tag{A6}$$

where Ω is the angular velocity of the turbine, and ω is the angular velocity induced to the flow by the turbine rotation. The TSR is defined as $\text{TSR} = R\Omega/U_\infty$, and the wake azimuthal velocity is defined as $V_\theta = \omega r$, then the thrust element, $\mathrm{d}T$, becomes

$$dT = 2\pi\rho\frac{\text{TSR}U_\infty}{R}\omega r\left(1+\frac{\omega r}{2\Omega r}\right)r^2\,dr = 2\pi\rho\frac{\text{TSR}U_\infty}{R}V_\theta\left(1+\frac{1}{2\text{TSR}}\frac{R}{r}\frac{V_\theta}{U_\infty}\right)r^2\,dr. \tag{A7}$$

Therefore, the thrust coefficient can be evaluated as

$$C_T = \frac{4\text{TSR}}{R^3}\int_0^R \frac{V_\theta}{U_\infty}\left(1+\frac{1}{2\text{TSR}}\frac{R}{r}\frac{V_\theta}{U_\infty}\right)r^2\,dr, \tag{A8}$$

By injecting Eq. (10) in Eq. (A8), it is obtained

$$\begin{aligned} C_T &= \frac{4\text{TSR}}{R^3}\int_0^R \left\{\Omega_{\text{hub}} r\exp\left[-\left(\frac{r}{\sigma_{\theta,\text{hub}}}\right)^\alpha\right] - \Omega_{\text{tip}}(r-r_{\text{tip}})\exp\left[-\left(\frac{r-r_{\text{tip}}}{\sigma_{\theta,\text{tip}}}\right)^\alpha\right]\right\} \\ &\quad\times\left(1+\frac{1}{2\text{TSR}}\frac{R}{r}\left\{\Omega_{\text{hub}} r\exp\left[-\left(\frac{r}{\sigma_{\theta,\text{hub}}}\right)^\alpha\right] - \Omega_{\text{tip}}(r-r_{\text{tip}})\exp\left[-\left(\frac{r-r_{\text{tip}}}{\sigma_{\theta,\text{tip}}}\right)^\alpha\right]\right\}\right) r^2\,dr \\ &= \frac{4\text{TSR}\Omega_{\text{hub}}}{R^3}\int_0^R \left\{r\exp\left[-\left(\frac{r}{\sigma_{\theta,\text{hub}}}\right)^\alpha\right] - k_\Omega(r-r_{\text{tip}})\exp\left[-\left(\frac{r-r_{\text{tip}}}{\sigma_{\theta,\text{tip}}}\right)^\alpha\right]\right\} \\ &\quad\times\left(1+\frac{\Omega_{\text{hub}}}{2\text{TSR}}\frac{R}{r}\left\{r\exp\left[-\left(\frac{r}{\sigma_{\theta,\text{hub}}}\right)^\alpha\right] - k_\Omega(r-r_{\text{tip}})\exp\left[-\left(\frac{r-r_{\text{tip}}}{\sigma_{\theta,\text{tip}}}\right)^\alpha\right]\right\}\right) r^2\,dr, \end{aligned} \tag{A9}$$

where $k_\Omega = \Omega_{\text{tip}}/\Omega_{\text{hub}}$.

[1] G. V. Iungo, Y.-T. Wu, and F. Porté-Agel, Field measurements of wind turbine wakes with lidar, J. Atmos. Ocean. Technol. **30**, 274 (2013).
[2] G. V. Iungo and F. Porté-Agel, Measurement procedures for the characterization of wind turbine wakes with scanning Doppler wind LiDARs, Adv. Sci. Res. **10**, 71 (2013).
[3] J. N. Sorensen, R. F. Mikkelsen, S. Sarmast, S. Ivanell, and D. S. Henningson, Determination of wind turbine near-wake length based on stability analysis, J. Phys.: Conf. Ser. **524**, 012155 (2014).
[4] S. Wharton and J. K. Lundquist, Atmospheric stability affects wind turbine power collection, Environ. Res. Lett. **7**, 014005 (2012).
[5] H. Quaranta, H. Bolnot, and T. Leweke, Long-wave instability of a helical vortex, J. Fluid Mech. **780**, 687 (2015).
[6] M. Felli, R. Camussi, and F. Di Felice, Mechanisms of evolution of the propeller wake in the transition and far fields, J. Fluid Mech. **682**, 5 (2011).
[7] W. Zhang, C. D. Markfort, and F. Porté-Agel, Near-wake flow structure downwind of a wind turbine in a turbulent boundary layer, Exp. Fluids **52**, 1219 (2012).
[8] M. Bastankhah and F. Porté-Agel, A new analytical model for wind-turbine wakes, Renewable Energy **70**, 116 (2014).
[9] L. P. Chamorro, C. Hill, S. Morton, C. Ellis, R. E. A. Arndt, and F. Sotiropoulos, On the interaction between a turbulent open channel flow and an axial-flow turbine, J. Fluid Mech. **716**, 658 (2013).
[10] S. Kang, X. Yang, and F. Sotiropoulos, On the onset of wake meandering for an axial flow turbine in a turbulent open channel flow, J. Fluid Mech. **744**, 376 (2014).
[11] K. B. Howard, A. Singh, F. Sotiropouloss, and M. Guala, On the statistics of wind turbine wake meandering: An experimental investigation, Phys. Fluids **27**, 075103 (2015).
[12] S. E. Widnall, The stability of a helical vortex filament, J. Fluid Mech. **54**, 641 (1972).
[13] V. L. Okulov, On the stability of multiple helical vortices, J. Fluid Mech. **521**, 319 (2004).
[14] V. L. Okulov and J. N. Sorensen, Stability of helical tip vortices in a rotor far wake, J. Fluid Mech. **576**, 1 (2007).
[15] H. Levy and A. G. Fordyke, The steady motion and stability of a helical vortex, Proc. R. Soc. Lond. A **120**, 670 (1928).
[16] B. P. Gupta and R. G. Loewy, Theoretical analysis of the aerodynamic stability of multiple, interdigitated helical vortices, AIAA J. **12**, 1381 (1974).
[17] S. Ivanell, R. Mikkelsen, J. N. Sorensen, and D. Henningson, Stability analysis of the tip vortices of a wind turbine, Wind Energy **13**, 705 (2010).
[18] G. V. Iungo, F. Viola, S. Camarri, F. Porté-Agel, and F. Gallaire, Linear stability analysis of wind turbine wakes performed on wind tunnel measurements, J. Fluid Mech. **737**, 499 (2013).
[19] F. Viola, G. V. Iungo, S. Camarri, F. Porté-Agel, and F. Gallaire, Prediction of the hub vortex instability in a wind turbine wake: Stability analysis with eddy-viscosity models calibrated on wind tunnel data, J. Fluid Mech. **750**, R1 (2014).
[20] F. Viola, G. V. Iungo, S. Camarri, F. Porté-Agel, and F. Gallaire, Instability of wind turbine wakes immersed in the atmospheric boundary layer, J. Phys.: Conf. Ser. **625**, 012034 (2015).
[21] V. L. Okulov, I. V. Naumov, R. F. Mikkelsen, I. K. Kabardin, and J. N. Sorensen, A regular Strouhal number for large-scale instability in the far wake of a rotor, J. Fluid Mech. **747**, 369 (2014).
[22] G. V. Iungo and F. Porté-Agel, Volumetric lidar scanning of wind turbine wakes under convective and neutral atmospheric stability regimes, J. Atmos. Ocean. Technol. **31**, 2035 (2014).
[23] G. V. Iungo, Experimental characterization of wind turbine wakes: Wind tunnel tests and wind LiDAR measurements, J. Wind Eng. Industr. Aerodyn. **149**, 35 (2016).
[24] X. Carton and J. McWilliams, Barotropic and baroclinic instabilities of axisymmetric vortices in a quasigeostrophic model, Mesosc./Synop. Coher. Struct. Geoph. Turbul. **50**, 225 (1989).
[25] R. Ashton, F. Viola, F. Gallaire, and G. V. Iungo, Effects of incoming wind condition and wind turbine aerodynamics on the hub vortex instability, J. Phys.: Conf. Ser. **625**, 012033 (2015).
[26] W. C. Reynolds and K. M. Hussain, The mechanics of an organized wave in turbulent shear flow. Part 3. Theoretical models and comparisons with experiments, J. Fluid Mech. **54**, 263 (1972).

[27] N. Reau and A. Tumin, On harmonic perturbations in a turbulent mixing layer, Eur. J. Mech. (B/Fluids) **21**, 143 (2002).
[28] C. Cossu, G. Pujals, and S. Depardon, Optimal transient growth and very large scale structures in turbulent boundary layers, J. Fluid Mech. **619**, 79 (2009).
[29] L. A. Martinez-Tossas, M. J. Churchfield, and S. Leonardi, Large eddy simulations of the flow past wind turbines: Actuator line and disk modeling, Wind Energy **17**, 657 (2014).
[30] L. P. Chamorro and F. Porté-Agel, A wind-tunnel investigation of wind-turbine wakes: Boundary-layer turbulence effects, Boundary-Layer Meteorol. **132**, 129 (2009).
[31] Y.-T. Wu and F. Porté-Agel, Large-eddy simulation of wind-turbine wakes: Evaluation of turbine parametrisations, Boundary-Layer Meteorol. **138**, 345 (2011).
[32] V. Kitsios, L. Cordier, J.-P. Bonnet, A. Ooi, and J. Soria, Development of a nonlinear eddy-viscosity closure for the triple-decomposition stability analysis of a turbulent channel, J. Fluid Mech. **664**, 74 (2010).
[33] S. B. Pope, *Turbulent Flows* (Cambridge University Press, Cambridge, 2000).
[34] Y.-T. Wu and F. Porté-Agel, Atmospheric turbulence effects on wind-turbine wakes: An LES study, Energies **5**, 5340 (2012).
[35] J. C. del Alamo and J. Jimenez, Linear energy amplification in turbulent channels, J. Fluid Mech. **559**, 205 (2006).
[36] T. Burton, D. Sharpe, N. Jenkins, and E. Bossanyi, *Wind Energy Handbook* (John Wiley & Sons, New York, 2001).
[37] F. Gallaire and J.-M. Chomaz, Mode selection in swirling jet experiments: A linear stability analysis, J. Fluid Mech. **494**, 223 (2003).
[38] G. Carnevale and R. Kloosterziel, Emergence and evolution of triangualr vortices, J. Fluid Mech. **259**, 305 (1994).
[39] P. Orlandi and G. Carnevale, Evolution of isolated vortices in a rotating fluid of finite depth, J. Fluid Mech. **381**, 239 (1999).
[40] J. N. Sorensen and G. A. M. van Kuik, General momentum theory for wind turbines at low tip speed ratios, Wind Energy **14**, 821 (2010).
[41] M. Calaf, C. Meneveau, and J. Meyers, Large eddy simulation study of fully developed wind-turbine array boundary layers, Phys. Fluids **22**, 015110 (2010).
[42] F. Porté-Agel, Y.-T. Wu, H. Lu, and R. J. Conzemius, Large-eddy simulation of atmospheric boundary layer flow through wind turbines and wind farms, J. Wind Eng. Ind. Aerodyn. **99**, 154 (2011).
[43] J. P. Goit and J. Meyers, Optimal control of energy extraction in wind-farm boundary layers, J. Fluid Mech. **768**, 5 (2015).
[44] J. Jonkman, S. Butterfield, W. Musial, and G. Scott, *Definition of a 5-MW Reference Wind Turbine for Offshore System Development*, Tech. Rep. NREL/TP-500-38060 (NREL Technical Report, National Renewable Energy Laboratory, Golden, CO, 2009).
[45] E. Kulunk, *Aerodynamics of Wind Turbines, Fundamental and Advanced Topics in Wind Power* (InTech, 2011).